AGU100 ADVANCING EARTH AND SPACE SCIENCE

Radio Science

TECHNICAL REPORTS: METHODS

10.1029/2018RS006617

Demonstration of a Broadband Very Long Baseline Interferometer System: A New Instrument for High-Precision Space Geodesy

A. Niell[1], J. Barrett[1], A. Burns[1], R. Cappallo[1], B. Corey[1], M. Derome[1], C. Eckert[1], P. Elosegui[1,2], R. McWhirter[1], M. Poirier[1], G. Rajagopalan[1], A. Rogers[1], C. Ruszczyk[1], J. SooHoo[1], M. Titus[1], A. Whitney[1], D. Behrend[3], S. Bolotin[3], J. Gipson[3], D. Gordon[3], E. Himwich[3], and B. Petrachenko[4]

[1]Massachusetts Institute of Technology Haystack Observatory, Westford, MA, USA, [2]Institute of Marine Sciences, ICM-CSIC, Barcelona, Spain, [3]NVI, Inc., Greenbelt, MD, USA, [4]Natural Resources Canada, Penticton, British Columbia, Canada

Key Points:
- We demonstrated the first broadband VLBI systems for high-precision space geodesy
- We developed procedures for data acquisition and analysis of the broadband geodetic data
- We generated the first VGOS baseline length time series

Correspondence to:
A. Niell,
aniell@mit.edu

Citation:
Niell, A., Barrett, J., Burns, A., Cappallo, R., Corey, B., Derome, M., et al. (2018). Demonstration of a broadband very long baseline interferometer system: A new instrument for high-precision space geodesy. *Radio Science*, *53*, 1269–1291. https://doi.org/10.1029/2018RS006617

Received 2 MAY 2018
Accepted 6 SEP 2018
Accepted article online 17 SEP 2018
Published online 4 OCT 2018

Abstract A prototype broadband geodetic very long baseline interferometry system has been implemented, and measurements of the baseline length over approximately two years, between December 2014 and January 2017, have been made in the process of exercising the system, developing operational procedures, and assessing geodetic precision for the new broadband observing concept. In addition to developing a broadband signal chain and installing the instrumentation on both a new 12-m antenna at the Goddard Geophysical and Astrophysical Observatory and the 18-m Westford antenna at the Massachusetts Institute of Technology Haystack Observatory, it was necessary to develop new correlation and analysis procedures to process the four-band, dual-linear-polarization data. A geodetic analysis of the data from 19 sessions that were observed during this period yielded a weighted root-mean-square deviation of the baseline length residuals about the weighted mean of 1.6 mm. These results validate several of the expectations set forth for the vision of the next-generation geodetic very long baseline interferometry system.

1. Introduction

The technique known as very long baseline interferometry (VLBI) was developed by radio astronomers in the late 1960s to attempt to resolve the compact radio emission from quasars and astronomical masers (e.g., Bare et al., 1967; Broten et al., 1967; Moran et al., 1967). The value of the technique for investigating a number of geophysical problems that require high-precision measurements, such as the determination of contemporary plate tectonic motions and variations in the Earth's orientation and rotation, was quickly pointed out and observations initiated (e.g., Carter et al., 1984; Gold, 1967; Herring et al., 1986; Hinteregger et al., 1972; Robertson, 1991; Robertson et al., 1983; Whitney et al., 1976). The development was symbiotic between geodesy and astronomy (e.g., Kellermann & Moran, 2001) because the technique relies on measuring the difference in the times of arrival at two antennas, which are tied to the surface of the Earth, of the microwave signals from a distant astronomical radio source (e.g., Thompson et al., 2017). The developments of VLBI and the complementary technique of satellite laser ranging (SLR) were approximately contemporaneous and were followed by the later addition of two more geodetic techniques: Global Navigation Satellite System (GNSS) and Doppler Orbitography and Radiopositioning Integrated by Satellite (DORIS). Collectively, these four systems constitute the so-called space geodetic techniques.

Space geodesy provides key measurements of geophysical characteristics of Earth from the ionosphere to the core and of the layers in-between (e.g., Davis et al., 2016). Space geodesy is also a critical science enabler in that it provides the supporting infrastructure for a wide variety of science missions and applications (e.g., Abdalati et al., 2018; Davis, 2010). One such critical contribution of space geodesy is the definition and realization of a terrestrial reference frame, which is a practical framework for describing the shape and orientation of the Earth as well as their temporal variations. A substantial number of geophysical problems, such as the measuring of global sea level rise from space-based altimeters, rely on the availability of accurate Earth coordinates (e.g., Abdalati et al., 2018).

VLBI contributes significantly to the International Terrestrial Reference Frame (Altamimi et al., 2016), which is the realization of the International Terrestrial Reference System (Petit & Luzum, 2010a), in particular for its scale, and uniquely to the realization of the International Celestial Reference System (Seidelmann & Kovalevsky, 2002). In addition, VLBI uniquely provides a full set of self-consistent Earth orientation parameters (EOP) that link the terrestrial and celestial frames together and enable Earth positioning and space navigation.

The precision of position estimates from VLBI has improved from a few meters in the 1970s to the subcentimeter level today. Although improvements in data processing methods and physical models (e.g., Petit & Luzum, 2010b) have contributed to this, a considerable number of technology improvements have been the main factors in enabling the 3-order-of-magnitude leap in precision (e.g., Sovers et al., 1998). These include the wide spanned bandwidths made possible by the so-called bandwidth synthesis technique (Rogers, 1970), a calibration system for instrumental delays (Rogers et al., 1983), dual-frequency observations to correct for all dispersive effects on the radio signal between the source and the antenna (primarily the Earth's ionosphere), and low-system-temperature cryogenic receivers. However, some of the most vital Earth problems, such as the melting of the polar ice sheets and sea level change, still require further improvements in precision, in particular for the International Terrestrial Reference Frame.

The primary focus of this article is to describe the development and preliminary realization of the next-generation VLBI system, the so-called VLBI Global Observing System (VGOS), which, together with the next-generation versions of the other space geodetic techniques, is being developed to meet the very stringent science requirements: an accuracy of 1 mm in station position and 0.1 mm/year in station velocity on global scales (Niell et al., 2006; Petrachenko et al., 2009). It is expected that VGOS will grow from the two-station interferometer demonstration in this study to a global network of 16 to 32 stations in the coming decade (Abdalati et al., 2018).

In the following, we sequentially describe the history and goals of VGOS, the antennas and associated broadband signal chain elements, the observations, data acquisition, extraction of the interferometric delay observable, and processing and analysis of the geodetic data, including a preliminary assessment of the precision of the length estimates of the VGOS prototype presented here. We close with some ideas about future work and the expectations for a global VGOS network.

2. VGOS System Requirements

Around the beginning of the new millennium, a number of scientific and technological factors converged to motivate consideration of a next-generation VLBI system for the global geodesy and astrometry network: (1) Emerging geodetic requirements were demanding a significant leap in VLBI performance; for example, (i) mean sea level studies demonstrated the need for 1-mm position accuracy on global scales; (ii) interpretation and verification of time series of EOP would benefit from having roughly uniform quality in the daily products from all techniques; (iii) operational requirements for universal time (UT1) demanded short latency between data acquisition and availability of the initial products. (2) Many of the network antennas were not designed for geodesy and astrometry but were aging second-use antennas and, consequently, were becoming more expensive to maintain, inefficient to operate, and a poor fit for modern geodetic VLBI observing programs. (3) Existing data acquisition systems, conceived in the 1970s, were becoming obsolete. (4) Radio frequency interference (RFI) was impacting observations and becoming a growing operational problem. (5) Technological advances in electronics, global optical network capacity, and low-cost antennas were presenting revolutionary new design opportunities.

Shortly before this, the efforts of the many cooperating groups that were providing these geodetic and astrometric results were organized under the International Association of Geodesy as the International VLBI Service for Geodesy and Astrometry (IVS), a new association through which the resources of the many independent groups could be coordinated and focused.

In 2003, the IVS formed a working group to define requirements for a next-generation geodetic VLBI system (initially called the VLBI2010 system but renamed VGOS in 2012). All aspects of VLBI systems and operations were reviewed within the working group, and bold goals were established for the new system: (i) 1-mm position accuracy on global scales, (ii) continuous measurement for time series of station positions and EOP, and (iii) turnaround time to initial products within 24 hours of collecting the data (Niell et al., 2006). Of the three

VGOS goals, the first is predominantly a performance-related goal, while the other two are more operational in nature.

Achieving the operational goals is comparatively straightforward. For example, continuous operation has been limited by the use of antennas that are in many cases shared with other applications, along with the high costs of data transfer and site operations. To solve these problems, new antennas are expected to be dedicated to VGOS and to employ enhanced automation and remote control, thus minimizing operation costs. At the same time, it was expected that commercial pressure would reduce network usage costs and increase data storage densities, both of which would reduce the cost of data transfer. With respect to the goal of short turnaround time to initial products, it was expected that the anticipated reduction in network usage cost would make it increasingly economical to transport VGOS data electronically, thus eliminating the delay incurred by physically shipping recorded media.

In contrast, achieving global-scale position accuracy at the 1-mm level is a challenge. It was widely understood that the dominant random errors in geodetic VLBI are due to variations in the propagation delay of the troposphere, drifts of the hydrogen maser reference frequency, and thermal noise in the delay measurement, while the dominant systematic errors degrading geodetic VLBI measurements are electronic biases, antenna deformations, and radio source structure (Petrachenko et al., 2009; Xu et al., 2016).

To better understand the impact of random errors on geodetic products, Monte Carlo simulations were performed that used realistic models for the troposphere delay variations, hydrogen maser frequency stability, and Gaussian-noise-like delay error (Petrachenko et al., 2009). Various strategies were tested to determine which were most effective for minimizing the impact of random errors on the geodetic products. By far the most effective strategy was to significantly increase the number of angularly well-distributed observations per unit time, with one observation every 30 s achieving the 1-mm performance target in the simulation results, largely attributable to enhanced atmospheric sampling.

Systematic errors, as considered in this paper, are those that vary smoothly on a time scale of tens of minutes or longer. They generally are not reduced by averaging repeated observations. Many of them have some dependence on the immediate environment, such as phase and delay variations due to temperature changes in the signal chain hardware, mechanical flexing of antenna cables, and antenna structure. Experience has shown that the signal chain and cable variations can be corrected with sufficient accuracy by the use of phase calibration and cable-delay-measurement instrumentation. The effects of structural deformations are expected to be mitigated by the mechanical stiffness of the antennas and, possibly, by structural modeling. The potential for significant phase variation with frequency, which can compromise the benefit of observing phase over a wide bandwidth, was recognized from calculations of source structure phase based on images from the geodetic VLBI program and simple models of component spectra. However, there was optimism that the problem could be made insignificant by the judicious selection of sources with simple structure, supplemented by improved source mapping to generate source structure phase corrections from the observations.

The question then became what system parameters would be required to achieve approximately one observation per 30 s with sufficient signal-to-noise ratio (SNR) on enough different sources spaced appropriately around the sky. The studies suggested this could be accomplished with fast-slewing antennas of sufficient sensitivity. In particular, it was found that antennas with a slew speed in azimuth angle of 12°/s, and an elevation angle slew speed of 6°/s could move from one scheduled source to the next in 25 s on average. Furthermore, a pair of antennas, each with a system equivalent flux density (SEFD) of 2,500 Jy (1 Jy = 1 Jansky = 10^{-26} Wm^{-2} Hz^{-1}) (which can be achieved, e.g., with a diameter of 12 m, aperture efficiency of 50%, and system temperature of 50 K) and recording with an instantaneous data rate of 16 Gbps (1 Gbps = 10^9 bits per second) would have the sensitivity to detect a 250-mJy source with an SNR of about 20 in 10-s integration, which allows in excess of 100 high-quality radio sources to be observed. (SEFD is the strength of a radio source that would double the system temperature if viewed in the main beam of the antenna.) The final requirement from the simulations is that a delay precision of less than 16 ps (1 ps = 10^{-12} s, which corresponds to a propagation length of approximately 0.3 mm) is sufficient at that SNR to not degrade the position uncertainty in the environment of the other random error sources. However, since the other errors are likely to be reduced in the future, either through improved hardware or by better modeling, the goal for the delay precision was set at 4 ps. To achieve this, a new frequency and delay determination scheme, referred to as broadband delay, was proposed. This new scheme could be realized by, for example, connecting the phase across four optimally placed

Figure 1. Photo of the 12-m-diameter VGOS antenna at the Goddard Geophysical and Astronomical Observatory site.

1-GHz bands in the frequency range of 2 to 14 GHz. Details of these studies and the ensuing recommendations can be found in Petrachenko et al. (2009).

3. The MIT-NASA VGOS Prototype Systems

Two proof-of-concept broadband signal chain systems were developed by the Massachusetts Institute of Technology (MIT) Haystack Observatory (hereafter Haystack for short) to address some of the key VGOS requirements above. The systems were designed, constructed, and installed on two antennas, the 5-m-diameter MV-3 antenna at the Goddard Geophysical and Astrophysical Observatory (GGAO) in Greenbelt, Maryland, and the 18-m-diameter Westford antenna at Haystack in Westford, Massachusetts. MV-3 had been first used as a mobile antenna for geodetic VLBI observations and was subsequently permanently installed at GGAO to participate in global geodetic VLBI sessions. Sufficient observations were made with the two proof-of-concept systems to validate the design of the signal chain components, to demonstrate achievement of group delay precision of a few picoseconds, and to justify proceeding to the prototype development.

The two essential factors that enable significant improvement in geodetic VLBI accuracy with the VGOS systems are (a) the capability of the antennas to move rapidly around the sky to sample the changing atmosphere delay and (b) the broadband signal chain to significantly improve the delay precision and sensitivity. In order to more fully demonstrate the anticipated results, an advanced, next-generation broadband signal chain was developed and utilized on a new 12-m antenna installed at GGAO in 2011 (hereafter referred to as the GGAO antenna) and on the Westford antenna.

The GGAO 12-m-diameter antenna (Figure 1), though it slews much faster than MV-3, still does not achieve the VGOS design goal. It was, however, the fastest commercially available antenna at the time that also satisfied the VGOS size and geodetic structural requirements. The characteristics of these antennas and the properties of the signal chain components are summarized here, with details provided in the following sections. The main components of the Westford signal chain are illustrated in Figure 2. (The GGAO signal chain is similar but currently lacks a cable delay measurement system [CDMS].)

The cryogenic dewar of GGAO is mounted near the top of the feed cone, just below the subreflector. It contains the dual-linear-polarization feed, two low-noise amplifiers (LNAs), and two injection couplers in front of the LNAs for the calibration signals. The phase- and noise-calibration signal generators, as well as ambient

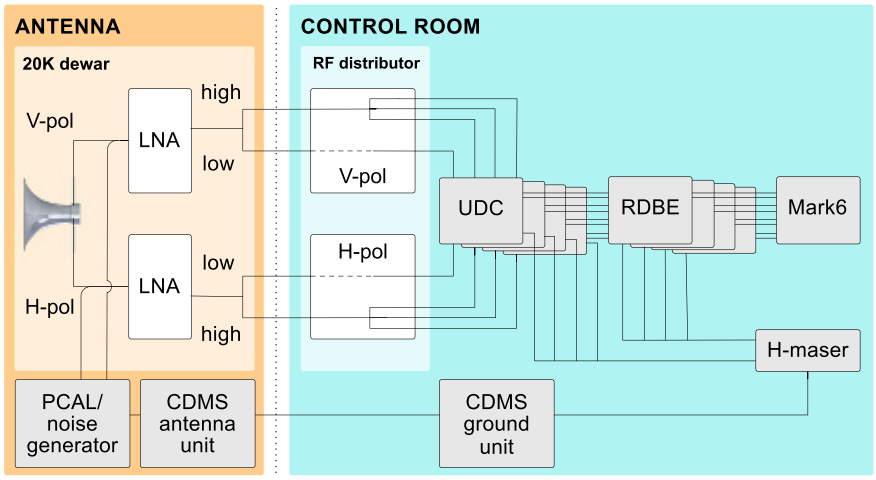

Figure 2. Block diagram of the broadband signal chain as implemented at Westford for VGOS observations. (See text for acronyms used.)

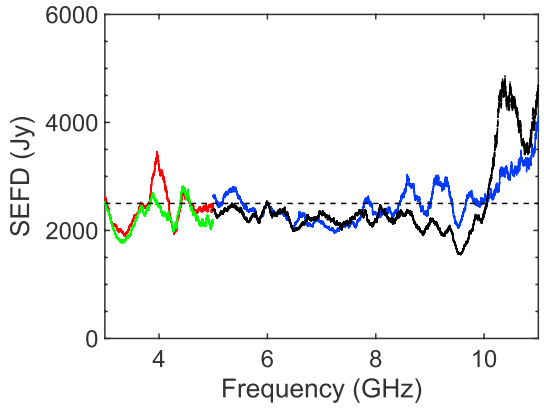

Figure 3. Radiometric performance of the GGAO antenna as characterized by its SEFD. The horizontal dashed line at 2,500 Jy is the VGOS specification. The data below 5.0 GHz are for the low-band signal path for (red) horizontal and (green) vertical polarization. The data above 5.0 GHz are for the high-band signal path for (blue) horizontal and (black) vertical polarization. The spike near 4 GHz in low-band/horizontal polarization is due to radio frequency interference of unknown origin. The increase in SEFD above 10 GHz is due primarily to diodes added in front of the LNA that protect them from damage by the 9.4-GHz aircraft avoidance radar at the nearby SLR station. SEFD = system equivalent flux density.

temperature amplifiers and filters, are mounted behind the dewar in the feed cone. The feed, the two LNAs (one for each polarization), and the couplers are cooled to approximately 20 K. After amplification, the radio frequency (RF) signal for each polarization is separated into two bands, a *high* band and a *low* band, and conveyed to the control room over optical fiber or coaxial cable. Unlike for GGAO, which is a Cassegrain antenna, for the Westford antenna all of these components are located at prime focus.

In the control room, the high band of each polarization is split three ways in the RF distributor, and each of the four RF signals (three high band and one low band) is passed to an up-down converter (UDC), which downconverts the signals. The two outputs of each UDC (one for each polarization) are digitized and formatted in a digital backend, and the digital signals from the four bands and two polarizations are recorded on one or more Mark6 disk modules (Whitney et al., 2013) at a rate of 8 Gbps. (Although the system is capable of utilizing the full 16 Gbps of information, only half is recorded, as explained in section 4.1).

The prototype systems differ in several respects from the VGOS goals. First, the antennas are not capable of the full slew rates specified to achieve the highest geodetic precision since they are limited to less than 5° and 3.5°/s in azimuth and elevation angle, respectively. Second, the frequency spanned by each of the four bands is only 512 MHz rather than the target of 1 GHz. And third, the VGOS sensitivity specification of 2,500 Jy is met only over the frequency range of 3 to 10 GHz.

3.1. Antennas and Optics

For both antennas, the linearly polarized feed was mounted such that the plane of one polarization contains the local topocentric vertical when the antenna is pointed near the horizon. The other polarization (horizontal) is orthogonal to this. The polarizations are thus referred to as *vertical (V)* and *horizontal (H)*.

3.1.1. GGAO Antenna

The 12-m-diameter Cassegrain-focus antenna at GGAO was manufactured by Patriot Antenna Systems. (Brand names are mentioned for identification purposes only.) The optics of the main surface and the 1.8-m subreflector, designed by Imbriale et al. (2007), achieve a maximum efficiency of better than 70% at frequencies below 4 GHz, dropping to 60% at 12 GHz. The effective focal-length-to-diameter ratio (f/D) for the dual-shaped-reflector system is 0.38.

The mount is elevation over azimuth, with elevation motion driven by a jackscrew. The elevation axis and azimuth axis were specified to intersect to less than 1 mm, but this has not been confirmed by additional measurements or by estimation from the geodetic VLBI data. Maximum slew rates in azimuth and elevation angles are 5°/s and 1.25°/s, respectively. The limits of motion are ±270° in azimuth relative to the neutral point to the east and 5.6° and 89.6° in elevation.

The noise contributions from the cooled feed and LNAs, plus atmosphere on a dry day and ground pickup, combine to produce a system temperature at zenith of less than 50 K, which, with an aperture efficiency of better than 60% over most of the range between 2 and 10 GHz, yields an SEFD of less than ~2,500 Jy for the frequencies used in the results reported here (Figure 3). The measurements were made using the strong radio source Cassiopeia A, while the elevation changed from approximately 36° to 30°.

3.1.2. Westford Antenna

The Westford antenna has been used as a dual-frequency S-band (2.2–2.4 GHz) and X-band (8.1–8.9 GHz) system from the inception of regularly scheduled geodetic VLBI S/X operations in 1980 (Carter et al., 1984; Robertson, 1991), giving it the longest measurement history of any geodetic VLBI antenna. The S/X receiver, and now the broadband receiver, are mounted at prime focus when in use. The two receivers can be exchanged over a 2-day interval, but the goal is to use only the broadband system for both S/X and VGOS measurements. The f/D ratio is 0.3. The slew rates are 3.5°/s in azimuth and 2.0°/s in elevation angle. The operational ranges in azimuth and elevation are +90° to +470° and 4° to 87°, respectively. The elevation axis is offset from the azimuth axis by 0.318 m. To protect the antenna surface and to improve efficiency in adverse weather

conditions, a radome covers the antenna and is attached to a concrete tower surrounding the mount. The reduction in RF signal power due to the radome is less than 0.2 dB when the radome is dry.

The Westford antenna was equipped with the broadband signal chain in order to provide a second element to demonstrate the interferometric capabilities of the GGAO 12-m system. While the efficiency of Westford is lower than for GGAO, the larger aperture and a comparable system temperature yield a similar sensitivity. With similar slew rates for the two antennas, the pair as an interferometer is not significantly limited in performance by either antenna.

3.2. Signal Chain Frontend

The frontend subsystem consists of the elements of the signal chain and monitor and control infrastructure (MCI) components that are mounted on the antenna. The signal chain components are the feed, phase, and noise calibration units; calibration injection couplers; LNAs; additional amplifiers and filters; and optical fiber link electronics for transmission of the RF signal to the control room, where the backend resides. The feed, LNAs, and associated couplers are mounted in a cryogenic dewar and cooled to approximately 20 K. At GGAO, the phase- and noise-calibration generators, additional amplifiers, coax-to-optical-fiber links, and MCI components are mounted on a tray to which the dewar is also attached. This structure rides on a motorized rail system inside the feed cone that allows adjustment of the position of the dewar for focusing and for lowering of the structure for maintenance. At Westford the frontend equipment is mounted at prime focus, and the position can be adjusted only manually.

The dewars were constructed at Haystack following a design by Imbriale et al. (2007). The two stages of cooling are at approximately 70 and 20 K. An important feature of these systems is the inclusion of the feed in the dewar to reduce its contribution to the system noise.

The feeds for both antennas, though slightly different in form, are of the Quadruple-Ridged Flared Horn style (Akgiray et al., 2013). The GGAO feed is circular and is designed to match the optics for which the 1.8-m subreflector is only 0.5 m from the feed. The Westford antenna, on the other hand, being prime focus with a relatively small f/D ratio of 0.3, requires a wider opening angle than does GGAO. To accommodate this different geometry, a special model of the Quadruple-Ridged Flared Horn feed was created. Even so, the main reflector is underilluminated, leading to reduced overall efficiency and an almost linear decrease from ∼50% at 3 GHz to ∼10% at 12 GHz.

The RF signal for each polarization is amplified initially by a broadband LNA for which the noise temperature is less than 7 K over the frequency range of 2 to 12 GHz.

Both antennas are equipped with phase and noise calibration systems. The phase calibration system generates very short ($\leq$50 ps) pulses at a 5-MHz rate that appear as phase-coherent tones throughout the frequency range of the receiver (see section 3.4.1). These tones are used to correct phase and delay errors introduced by the instrumentation. (The phase calibration signal will be referred to as *phasecal* in the frequency domain and as *pulsecal* in the time domain and the noise calibration signal as *noisecal*.) The main purpose of the noisecal generator (see section 3.4.3) is to provide a stable, broadband noise signal to which measurements of the system noise can be referred to provide accurate measurement of system noise temperature and, ultimately, correlated flux densities of the radio sources.

The phasecal and noisecal generators are mounted in a common, thermally insulated, temperature-stabilized, RF-tight enclosure. The outputs of both are split, then one output from each is fed to one of two combiners, and the outputs of the two combiners are fed into the dewar. Inside the dewar, each of the combined calibration signals is added to one of the two polarizations through a −20-dB coupler (Figure 2). Although it would have been less expensive to downconvert the RF to lower frequencies at the antenna and transmit the signals to the control room over eight coaxial cables, this was not feasible because of (a) the limited space in the pedestal of the antenna that was selected and (b) the resulting requirement for temperature control of the signal chain components in the ambient environment. Thus, it was decided to carry the signals over optical fibers (Welch et al., 2009). However, due to the limited dynamic range of the optical fiber transmitters and the presence of strong RFI in the lower range, it became necessary to separate the signals into higher and lower ranges. To accomplish this, the RF signals are carried from the antenna frontend to the control room at Westford over separate optical fibers for the high-band (>5 GHz) and low-band (<6 GHz) ranges. At GGAO, where the cable run is shorter, fiber is used for frequencies greater than 4 GHz and coaxial cable for frequencies below 5 GHz.

3.3. Signal Chain Backend

The backend subsystem consists of all components of the signal chain in the control room, where the RF signals are further amplified and separated into bands in the RF distributor, downconverted, digitized, formatted, and recorded (Figure 2).

3.3.1. RF Distribution

The primary role of the RF distributor is to provide four RF signals per polarization that, following downconversion and band-pass filtering in the following UDCs, become the four frequency bands that are digitized and recorded. (The bands are designated A through D from lowest to highest frequency.) The lowest band of each polarization, being on a separate line from the frontend, is passed through the RF distributor, while the high band is split three ways. Each RF path is amplified and has the provision for injection of a test signal. The same couplers that are used for the test signal injection allow monitoring of the RF signal.

3.3.2. Frequency Downconversion

The RF signals for both polarizations of each band are translated to an intermediate frequency (IF) in the same UDC. In each UDC the frequency band is selected by a first mixer stage with a tunable local oscillator (LO) synthesizer that moves the desired input frequencies up to 20–22 GHz. The signal passes through a 2-GHz band-pass filter with high out-of-band rejection and is then downconverted to 0.5–2.5 GHz in a second mixer stage with fixed LO at 22.5 GHz. The appropriate power level is obtained by amplifiers and a tunable attenuator. Finally, the signal passes through a filter (which passes approximately 512 to 1024 MHz), appropriate to the second Nyquist zone for the 1,024 megasamples per second (Msps) sample rate of the digital backend.

3.3.3. Digitization and Formatting

The downconverted signals are digitized and formatted in the geodetic version of the Reconfigurable Open Architecture Computing Hardware (ROACH) digital backend (RDBE-G), which is an enhanced version of the RDBE-H (Niell et al., 2010). Additional features, such as extraction of the temporal profile of the pulsecal signal and internal timing measurements, were implemented in the RDBE-G to satisfy the needs of geodetic VLBI.

The principal components of the RDBE-G are a 1024-MHz synthesizer, two analog-to-digital converters, and the high-speed ROACH digital signal processing board. The synthesizer board (Rogers, 2006) uses a 5-MHz reference signal from the hydrogen maser to generate a 1024-MHz clock signal to drive the samplers. It also buffers the maser and Global Positioning System (GPS) 1 pulse-per-second (1-pps) input signals.

The two 512-MHz-wide IF signals (vertical and horizontal polarization) from one UDC are input to an RDBE and sampled with 8-bit resolution at 1,024 Msps. Each sampled signal is channelized into 16 channels of 32-MHz bandwidth in a digital polyphase filter. The samples are then reduced to a 2-bit representation and assembled into VDIF (VLBI Data Interchange Format) packets (Whitney et al., 2010) for transmission to the Mark6 or other recorder. All or a subset of the 16 channels for each IF can be selected to be transmitted. The pulsecal signal is extracted prior to channelization.

A 1-pps signal is generated in the RDBE firmware. An external 1-pps signal from the hydrogen maser is used to set the initial alignment of the internal 1-pps signal, usually only at power-up of the RDBE. The offsets of the internally generated 1-pps signal relative to the maser 1-pps and to the GPS 1-pps signals are measured in the RDBE and displayed on a front panel. The values are also logged at the time of each scan during a session. (See section 3.5 for details of the timing requirements for correlation.)

3.3.4. Mark6 Data Recorder

The Mark6 VLBI data recorder (Whitney et al., 2013) was designed specifically to support VLBI systems that require the recording of a single continuous digital data stream at a rate of up to 16 Gbps. It utilizes commercial off-the-shelf technology for all data handling hardware, including modern high-performance motherboards and disk controllers. The software operates under a fully open-source Debian Linux distribution with open-source application software written primarily in C for the data handling and Python for the command and control interface.

Data input to the Mark6 is through four 10GigE ports, any combination of which may be utilized. Each port can operate independently and continuously at up to ~7 Gbps with a maximum average aggregate rate of ~16 Gbps when using all four input ports. Data are written to (up to) four removable 8-disk modules. Each module is connected to a disk controller via two standard external SATA (Serial AT Attachment) cables. Depending on the data recording rate, different numbers of simultaneously operating modules are utilized. A single 8-disk module will support continuous recording at up to 4 Gbps, while two modules (16 disks) are required for continuous 8 Gbps recording, and four modules (32 disks) are required for continuous 16 Gbps recording.

The VGOS observing sessions described here used scans that were mostly 30 s in duration. The scans were separated by a slightly larger time interval, during which the antenna moved to another radio source in a different part of the sky. Since data may be captured in Mark6 random access memory at a higher rate than can be recorded to the 8-disk module, the large amount of high-speed random access memory available on the Mark6 motherboard allowed completion of the transfer of the captured data for each scan to a single module before the next scan began. For the VLBI sessions reported here, each of the RDBE-Gs fed the Mark6 through one 10GigE port, and all of the data for each station were recorded on one 8-disk module having a total capacity of either 16 or 32 TB.

3.4. Calibration Systems

The phasecal and noisecal generators provide the fundamental calibration signals for the geodetic (delay) and astronomical (correlated flux density) products of the VLBI system.

3.4.1. Phase Calibration System

The primary role of the phasecal system is to measure any nonlinearities or temporal variations in the phase-versus-frequency response of the signal chain following the feed in order to provide correction of the observed phases following correlation. This is accomplished by generating and injecting near the feed a train of narrow pulses with a repetition rate of 5×10^6 pulses per second (5 Mpps) (Figure 2). When injected into the frontend, this signal allows variations in instrumental phase to be measured every 5 MHz over the full range. Delay variations can be computed from these phases but with an ambiguity of 200 ns (1 ns = 1 nanosecond = 10^{-9} s) due to the 5-MHz spacing at which the phases are measured. The Fourier transform of this pulse train is a sequence of tones at multiples of 5 MHz extending in frequency from below 2 to above 14 GHz. The phases and amplitudes of all tones are extracted in the correlator.

The phasecal generator used to create these signals is a digital replacement for the Mark3 phasecal unit (Rogers et al., 1983). The new design features 5-MHz tone spacing, less loss of power at the higher frequencies, and a very low coefficient of phase change with temperature. Compared with the 1-Mpps rate of the phasecal systems used in most S/X geodetic observations, the use of 5 Mpps is advantageous in a broadband system (Rogers, 2008, 2009). By increasing the pulse rate by a factor of 5 and reducing the pulse amplitude by the same factor, the tone amplitude is left unchanged, but the risk of the pulse saturating the electronics is greatly reduced.

Even with the wider spacing of 5 MHz between tones, compared to 1 MHz for the S/X systems, there are 6 or 7 tones present in each 32-MHz-wide channel, which is more than sufficient to estimate the instrumental delay in each channel to sub-nanosecond precision with less than 1 s of integration.

The phasecal delay is calculated in *fourfit* as a linear fit to the phasecal phases with frequency for each channel and is referred to as the *phasecal multitone delay* (Cappallo, 2011). The phase value used to correct each channel is the phase evaluated at midband. Both the phasecal multitone delay and the phasecal phases are used in *fourfit* to align the phases of the four bands of the broadband system, which is done separately for each polarization product.

High stability of the timing of the phase calibrator pulses is essential to achieving the VGOS accuracy goals. In order to maintain pulse delay variations under 1 ps, the temperature of the calibrator is stabilized with a Peltier temperature controller. The measured temperature sensitivity of the pulse epoch from the calibrator is 0.0 ± 0.5 ps/K (Rogers, 2015).

3.4.2. The 5-MHz Cable Delay Determination

The temporal stability of the phasecal pulses is also affected by delay variations in the coaxial cable carrying the 5-MHz reference signals from the maser to the phasecal generator. (Note that this is a different cable from the low-band coax bringing the RF down at GGAO.) These variations may be thermally driven or mechanically induced, for example, by stretching or twisting in the cable wraps around the antenna axes as the antenna slews. The latter are of particular concern because a variation that is correlated with antenna orientation will introduce a systematic error in the site position estimate. If the dependence on orientation of the variation does not change from session to session, the effect is a constant error in the estimated position of the antenna, thus affecting position accuracy. If the variation does change between sessions, the estimated position will also vary, thus affecting position repeatability. It is therefore critical, for geodesy, to measure with picosecond precision any change in the delay of the cable that carries the frequency reference signal that drives the phasecal generator. Such a measurement system is referred to as the CDMS or, for the S/X systems, *cablecal*.

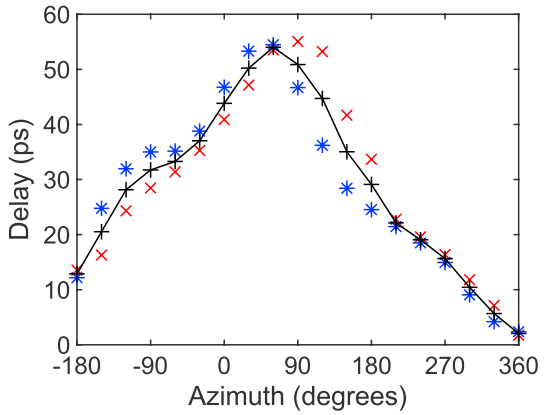

Figure 4. Observed GGAO phasecal multitone delays for bands B–D as the antenna was slewed in azimuth. Median values for four consecutive slews are shown every 30° for (red x) clockwise and (blue *) counterclockwise motion, and (black + and line) their mean value.

A CDMS that can determine the one-way travel time through the 5-MHz cable with subpicosecond precision was in development as part of the broadband signal chain, but it had not been completed by the time the other components were installed at GGAO and Westford and were ready for observation. However, an older Mark3 cablecal system, which has the same functionality, became available at Westford starting in 2016.

In order to assess the character and magnitude of possible delay variations in the cable carrying the 5-MHz reference to the phasecal generator at GGAO, measurements of the round-trip delay in each band were made while moving the antenna in azimuth and elevation in a controlled way. The delay was obtained from the phasecal tones across the full band, which, as noted above, reflects the phase change from the 5-MHz origin to the point of phasecal injection and the changes for each band from that point down the signal chain to digitization. From these measurements, it was apparent that for GGAO the phase and delay characteristics of band A, which is carried over a coaxial cable, are typically quite different from bands B–D, which are very similar to each other for both polarizations and both directions of azimuth and elevation motions. Since changes in the 5-MHz cable should affect all bands the same way, it was concluded that the bands B–D delays are more indicative of the variations in the 5-MHz cable and should be used without band A.

During the time of the early observations for GGAO (i.e., prior to June 2015), the delay variations in azimuth and elevation were very small, less than a few picoseconds. After June 2015 the azimuth dependence increased significantly, reaching a peak-to-peak range of almost 100 ps over the 540° range of the azimuth cable wrap. An example is shown in Figure 4. Subsequent to the observations reported here, inspection of the coaxial cable carrying the 5-MHz signal to the phasecal generator revealed that it was severely damaged. It was replaced, and the azimuth dependence returned to the early small variation.

Since no CDMS is yet available at GGAO, nor was one available for Westford before 2016, a proxy for the measurement was obtained as follows. While delay variations that originate after the phase calibrator injection point can differ among channels, bands, and polarizations, delay changes due to variations in electrical length of the 5-MHz reference cable are common to all bands and polarizations, as mentioned above. Thus, subtraction of the phasecal phases across all bands and polarizations both corrects for the instrumental phase errors (as desired) and introduces the 5-MHz cable delay changes (not desired). However, the latter would normally be removed by application of the CDMS values at the geodetic analysis stage. Lacking a CDMS, advantage can be taken of the inclusion of the cable delay in the multitone delay for each band. By calculating for each scan the multitone delay for each band and averaging over bands, an estimate of the 5-MHz cable delay plus the average of the instrumentation delay over those bands is obtained. Subtraction of this delay from the group delay for that scan then removes the cable delay (normally done by the CDMS) but actually reintroduces the average instrumentation delay. However, since the variation of the instrumentation delay, caused primarily by thermal effects, is expected to have a characteristic time scale of 30 min or more, it is absorbed in the estimation of the clock variation for each station in the geodetic estimation procedure. It is still necessary to apply phasecal to correct for band-to-band temporal variations, such as those due to LO phase drifts in the UDCs.

The main evidence that the cable delay proxy functions as expected is found in the geodetic analysis (see section 6). Incorporation of the proxy delay for GGAO both reduces the weighted root-mean-square (WRMS) postfit delay residual for the majority of sessions and decreases the scatter in the estimated lengths. For Westford, for sessions in which the CDMS was functional, the length difference between using the CDMS and using the proxy is less than 0.5 mm.

A shortcoming of the proxy approach can be illustrated in the session designated V16019 (Table 1) by comparison of the results for Westford using the proxy delay and the Mark3 CDMS delays. While the length estimate using the proxy delays is within 0.5 mm of that with the CDMS, the scatter of the delay residuals within the session is larger with the proxy, 10.6 ps, compared to 8.8 ps with the CDMS. However, this is attributable to an unusually rapid temperature variation of the UDCs at Westford, on a time scale comparable to the clock-estimation interval, which resulted in excess noise being added to the delays.

Table 1
Observing Sessions of the VGOS Demonstration Series

Date (yyyy/mm/dd)	Session name	Duration (h)	Scans observed	Scans used	WRMS ($\chi^2_\nu > 1$; ps)	Added noise (ps)	WRMS ($\chi^2_\nu = 1$; ps)
2014/12/19	V14353	1	58	57	6.2	10.1	7.8
2015/01/20	V15020	1	57	56	3.6	10.4	7.9
2015/02/03	V15034	1	50	50	4.0	13.8	10.5
2015/02/19	V15050	1	81	80	7.3	13.7	11.1
2015/03/03	V15062	1	67	67	3.4	9.4	7.4
2015/03/18	V15077	1	65	64	8.2	15.8	12.5
2015/04/28	V15118	1	61	59	6.2	12.7	9.9
2015/05/12	V15132[a]	1	58	54	10.8	28.0	21.6
2015/05/26	V15146[b]	4	153	148	18.6	34.1	29.3
2015/11/24	V15328	5	222	217	7.4	15.3	13.4
2015/12/08	V15342[c]	24	941	919	5.6	10.0	9.4
2016/01/19	V16019	1	57	57	4.6	13.7	8.8
2016/02/03	V16034	1	39	46	3.2	7.0	5.6
2016/08/11	VGT003	24	1,173	1,137	17.9	27.4	25.1
2016/08/30	VGT004	24	1,267	1,238	15.2	19.1	17.5
2016/11/15	VGP004	24	1,185	1,144	9.8	15.6	14.1
2016/11/29	VGP005	24	1,197	1,138	12.4	21.0	19.1
2016/12/19	VGP006	24	1,199	1,182	3.7	5.2	4.9
2017/01/17	VT7017	24	1,207	1,148	11.3	19.6	18.2

[a]There were no data from horizontal polarization, band A, at Westford. [b]The polarizations were crossed for bands B–D at Westford but corrected at the correlator. [c]Only 19 hr were used for the geodetic solution.

3.4.3. Noise Calibration System

The noisecal system injects broadband noise between the feed and each LNA to enable measurement of the system temperature T_{sys} (see, e.g., Thompson et al., 2017). The noise is generated by a diode that can be switched on and off at a selectable rate in the range 10 to 100 Hz. It is driven by the RDBE and, for these observations, was switched in synchronism with the 1-pps signal at a rate of 80 Hz with a duty cycle of 50%.

Demodulation of the total power in each channel is carried out in the RDBEs, and the diode *on* and *off* power levels, from which T_{sys} can be calculated, are integrated for each second and then multicast, that is, broadcast over the internal network. The rapid on-off signal switching mitigates the effects of drifts in system gain or in antenna temperature due, for example, to clouds or RFI. The strength of the calibration signal, T_{cal}, can be measured to an accuracy of approximately 10%, using an absorbing load over the feed, when the calibration signal power is approximately 5% of the system temperature. This is also the accuracy of the absolute T_{sys} measurements.

To this point the T_{sys} values in each band and polarization have been of use only to verify that the systems are working or to detect problems. In the future the measurements will be crucial for the calculation of correlated flux density in each band.

3.5. Time and Frequency

A unique product of geodetic VLBI is the measurement of the Earth's rotational phase—or, equivalently, time—with respect to the Celestial Reference Frame. To be useful, it is necessary to accurately relate that time to civil time—customarily Coordinated Universal Time (UTC). This is accomplished by establishing the time at each VLBI station relative to UTC via a GPS clock. Time accuracy through the VLBI session is maintained by the use of a stable frequency standard—a hydrogen maser—from which a reference frequency is derived for use in time tagging the data samples.

There are therefore two UTC-related reference signals, one each from GPS and from the hydrogen maser. The relation to UTC for each session is obtained through the GPS clock receiver. The GPS clock provides a 1-pps signal synchronized to UTC from the U.S. Naval Observatory master clock with an accuracy of better than

100 ns. The second signal of importance is the 1-pps time tick that is output from the maser. This signal, which is much more precise and stable than the GPS 1-pps signal, is initialized by triggering on the GPS signal at some instance prior to the VLBI session, perhaps even months before.

The 1-pps and reference frequency signals from the maser are crucial for precise data time tagging, which occurs in the RDBEs (see section 3.3.3). The maser 1-pps signal is used to provide to the RDBEs a synchronization signal to initialize a 1-pps counter, again at some time prior to the VLBI session, and the time in the RDBE is continued by counting cycles of the reference frequency from the maser, thus providing for the recorded data time tags that have the stability of the maser. The RDBEs continuously monitor the time differences between the RDBE 1-pps signal and the 1-pps's of both the maser and GPS. The offset of the RDBE 1-pps signal from the GPS 1-pps signal at the beginning of a session is used at the time of correlation for initial setting of the station clock. The offset of the RDBE 1-pps signal from the maser 1-pps signal is monitored to ensure that the RDBE remains locked to the maser.

For the reference frequency, a minimum stability is needed on two different time scales. At short times, up to the length of a scan, which can be up to 30 s, the stability must be sufficient to produce no significant loss of coherence at the highest observing frequency; this corresponds to an Allan deviation of about 1×10^{-14} at 30 s. At longer time scales the stability must be good enough that temporal variations in the time-base generated from the reference frequency do not add significant noise to the delays. To keep such noise below a few times the median per-scan delay uncertainty of ~4 ps, the stability should be better than approximately 1×10^{-14} at 1,200 s.

The VLBI2010 studies (Pany et al., 2011; Petrachenko et al., 2009) indicated that a combined stability of approximately 10^{-14} at 50 min (modeled as equal parts of random walk and integrated random walk; Herring et al., 1990) for the two stations forming a VLBI baseline is sufficient for the frequency reference to not be a limiting error source.

These stability requirements refer to the cumulative effect of the frequency reference signals as utilized by the various components of the VLBI system at each antenna, not just the output of the maser. While the performance of most masers is comfortably better than all three of these requirements, care must be taken that other components do not degrade the quality of the reference signals where applied. (Note that the requirement is on the frequency stability, not the absolute value of the frequency.) Also, it is important to understand that the same reference frequency signal is common to all components of the signal chain, that is, the phasecal, the CDMS, the LOs (in the UDCs), and the digital backends, in order to maintain phase stability and coherence throughout the system.

3.6. Monitor and Control Interface

The design goals for the MCI are (a) the ability to obtain information on all essential quantities that are needed for unattended operation of a VLBI station and (b) the ability to provide control of those items that are needed for operations or safety. These include both VLBI equipment and station environmental conditions. Five MCI nodes are planned, although not all have been implemented. The planned nodes are frontend, time and frequency, antenna, control room, and ancillary. The central component of each node is a headless computer system, which communicates via Ethernet to all of the associated sensors and which stores the data locally so that the values are available for later retrieval. Most of the sensors can be queried directly as well. For example, the Field System (FS; see below) can request values for, among others, meteorological conditions, the cable delay (at Westford), UDC frequencies and attenuations, and dewar temperatures and pressure. Other values, such as the time offsets of all four RDBEs from GPS and from the maser, are displayed in the control room in real time to provide monitoring of the health of the system.

The states of several components in the frontend are monitored or controlled remotely through the MCI. The most important of these are related to the helium supply for the cryogenic refrigerator and to the physical conditions (temperature and vacuum level) in the dewar. Outside the dewar the voltages, currents, and temperatures for the LNAs, calibration box, and compressor are monitored. The state of the noise diode, whether on or off, and the rate of switching can be controlled.

3.7. The Field System

The control system used for broadband observing is an extension of the standard National Aeronautics and Space Administration FS. Due to the requirement to make simultaneous observations at multiple globally dispersed antennas, operations at the different stations are coordinated through creation of an observation schedule (see section 4.2) and execution of the schedule commands by the FS at each station.

The VLBI schedule file is translated into station-specific commands that control the antenna, configure and monitor the station equipment, and start and stop recording of the data. The FS writes a log file that contains a record of all actions requested by the schedule, all responses from the instrumentation and the antenna, and any ancillary data, such as the 1-s digital counts of noise diode off and on total power, the derived system temperature, extracted phasecal information, and meteorological data. The FS also provides tools for the local station that can, for example, determine pointing corrections, measure the antenna gain, and plot various system parameters for easy visualization.

FS innovations for the VGOS demonstrations include parallel monitoring and control of multiple digital backends, UDCs, and Mark6 recorders. Newly developed FS support capabilities for the RDBE-Gs include making use of the continuous radiometry for pointing, antenna gain, and system temperature measurements.

The radiometric capabilities of the FS have been used at Westford and GGAO to generate improved antenna pointing models. The tracking accuracy is now better than 8 millidegrees for each axis, or, equivalently, less than 1/20th of full width at half maximum of the antenna beamwidths at the 10.2-GHz sky frequency for which the pointing offsets were measured. Any resulting loss of sensitivity is less than 1% for the VGOS 10-GHz band (band D).

Station-independent procedures were developed for the FS to set up the broadband system, verify its readiness for observations, run the schedule, monitor the operation, conclude the schedule when the session finishes, and transfer the VLBI data and log file for later analysis.

4. VGOS Demonstration Series

In December 2014 a series of biweekly observing sessions using Westford and GGAO was initiated to develop and demonstrate VGOS operational procedures. Table 1 lists the sessions observed in this VGOS demonstration series. Because VGOS is a significant innovation relative to the standard S/X geodetic VLBI system, hereafter referred to as *legacy VLBI* (e.g., Schuh & Behrend, 2012), major changes and additions have been required in the programs and scripts for the data flow and analysis. These include changes in scheduling to account for higher data rates; in correlator software to process new data formats, to handle complex samples, and to correlate the four bands simultaneously; in correlator post-processing software to apply the phasecal multitone signals, to coherently combine all bands and polarizations, and to simultaneously estimate the broadband delay and phase dispersion parameters; and in the database handler and geodetic parameter estimation software to process the broadband delay. These are described in the following sections.

4.1. VGOS Observing Frequencies

Numerical studies (Petrachenko, 2008; Petrachenko et al., 2009) conducted to determine the optimum configuration for band-frequency allocation of the broadband system indicated that using four 1-GHz bands gives a robust estimation of the delay. The use of fewer bands (two or three) increases the minimum SNR required for unambiguous detection of the group delay by 10% or more, while more bands do not provide any improvement. It was also shown that the precision of the delay estimate increased as the spanned frequency range increased. The choice of band frequencies was guided by limitations of the prototype instrumentation on the antennas. To obtain the smallest delay uncertainty, it was desirable to maximize the spanned bandwidth, subject to avoiding RFI that would severely impact the performance. Measurements of RFI indicated that frequencies below about 2.7 GHz would be affected, so a practical choice based on filter availability was to use a minimum frequency of 3.0 GHz. At the high end of the available frequency range the SEFDs of the antennas increased sharply above about 10.5 GHz, so the upper frequency was set to 10.7 GHz. As a result of simulations using 512-MHz bands (since the RDBE-G is not capable of 1-GHz bands), the frequencies of the two intermediate bands were selected to minimize the group delay uncertainty when estimating both the delay (phase proportional to frequency) and dispersion term (phase inversely proportional to frequency; see section 5.2.2). The center frequencies of the four 512-MHz bands were selected to be approximately 3.2, 5.5, 6.6, and 10.4 GHz.

Within each band only half of the available channels are recorded. This was done for the practical reason of recording only 8 Gbps on to one module in order to minimize the investment in media and to reduce shipping costs. The channel frequencies were chosen to provide a minimum-redundancy sequence with respect to the channel separations (Robertson, 1991; Rogers, 1970). With the frequencies of eight channels to be selected from 15 positions (channels 1 through 15) there are multiple configurations that cover all spacings between channels. The group delay uncertainty for an individual band can be minimized by selecting a configuration

with the most channels near the edges of the band. Further optimization can be obtained by retaining the channels that provide the most spacing redundancy. Any channel that contains strong RFI should be excluded and the channel-frequency distribution reconsidered. For all sessions the sequence {1,2,3,5,10,12,14,15} was used for each of the bands. For example, the lower edge frequencies of these channels for band A are 3.000, 3.032, 3.064, 3.192, 3.288, 3.352, 3.416, and 3.448 GHz.

4.2. VGOS Observations

The sequence of sources observed during a VLBI session is generated using the program *sked* (Gipson, 2012; Gipson & Baver, 2016), which is widely used within the IVS community to schedule geodetic and astrometric observations.

The unique inputs to sked for each session are the participating antennas and the time interval of the session. Parameters describing the properties of the antennas, such as sensitivity and the range and rate of motion, the radio sources available for observation, and the recording capability at each antenna, are selected from a set of catalog files.

Other parameters that determine the order of sources observed include the minimum required SNR for each scan and the minimum elevation to which the antennas can observe. For these sessions the minimum elevation was set to 5° for Westford and 6.25° for GGAO.

The minimum SNR per band was chosen to be 15 in order to make use of as many sources as possible. However, most scans would have a duration of less than 30 s for the sensitivities of the broadband systems, so the minimum scan length was set to 30 s to ensure high SNR and to limit the scan rate to approximately one per minute. The latter limitation was imposed to reduce the amount of movement of the two antennas in consideration of the age of Westford and the untested durability of the GGAO antenna.

The program *sked* is well developed for the legacy VLBI observing sessions, but it has been necessary to make changes to it to accommodate the new capabilities of the broadband system. The principal change required for the VGOS observations was to allow for the much higher record rate of the Mark6 compared to the maximum of 2 Gbps for previous recorders. To achieve this, a section was added that accepts three parameters per station: IF bandwidth, total input record rate, and maximum output rate to the recorders. The two record rates are required for sked to be able to calculate the minimum time before the next scan begins, since it must take into account the drain time when data are written to the disks at a lower rate than the data are taken in. This situation applies for VGOS data taken at 8 Gbps but written out to a single 8-disk Mark6 module. This limitation is not applicable at 8 Gbps when two or more 8-disk modules are available for recording.

Several additional changes to *sked* are still needed. Since there are four bands for VGOS instead of the two for S/X, the use of correlated flux densities and antenna sensitivities at all four bands should be implemented in order to calculate the scan length needed to achieve the minimum SNR for the weakest band. Another addition that is expected to be of benefit is the capability to schedule observations at fixed scan intervals with two to four radio sources visible for each scan and spaced approximately uniformly around the sky (Sun et al., 2014).

A major impact on the quality of the schedule is the need at GGAO to avoid pointing in the direction of either of the two SLR systems, which are located approximately 175 m to the southwest of the VGOS antenna. Associated with each of the SLR systems is a high-power 9.4-GHz aircraft avoidance radar that is capable of damaging the LNAs of the VLBI receiver if the radar and VLBI antenna are pointed too closely to each other. Through careful measurements of the power response pattern of the VLBI system and the power pattern of the SLR radar, a region of avoidance was derived for each system (basically a cone around the direction to the other site) that should avoid damage to the LNAs while maximizing the sky coverage for the SLR systems. The loss of area of the sky for the VLBI antenna is clear from the depiction of the azimuths and elevations of observations for a 24-hr schedule as shown in Figure 5. The significance of the lost area is that the sensitivity for the horizontal component of the station position is reduced by approximately 20%. To recover this sensitivity, the observing time along that projection would have to increase by 40%. In particular, this direction corresponds to the orientation of the GGAO-Westford baseline so the loss of data directly affects the precision of the length estimates.

Perhaps more significant is that the available common sky visibility with other VLBI antennas that lie within the cone of avoidance toward the SLR system is seriously reduced. For GGAO this will include the VGOS antenna at McDonald Observatory, Texas, currently under construction. However, this is a serious issue that should be

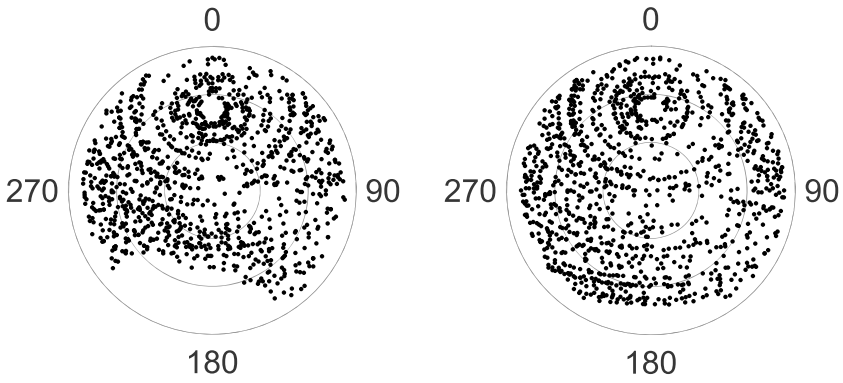

Figure 5. Example of azimuth and elevation angle polar plots of the directions of all observations at Goddard Geophysical and Astrophysical Observatory, here for 8 December 2015. Two schedules were made: (left) the directions close to the satellite laser ranging systems were masked out to reduce the risk of damage from the satellite laser ranging radar and (right) no mask was imposed. Zenith direction (i.e., 90° elevation angle) is at the center; the horizon is at the outer edge.

considered for all core sites of the Global Geodetic Observing System network where VLBI, SLR, GNSS, and DORIS are to be collocated.

All sessions reported here were scheduled with the SLR mask in place.

Other ways to mitigate the sensitivity of the VLBI systems to the SLR radar are being investigated, including coordinated observing to allow observations closer to the direction of the other system when the radar is pointing away from the VLBI antenna, and the addition of an RF filter in the VLBI frontend between the feed and the LNAs that would effectively block out the radar signal.

Blocking out the area of the sky in the direction of the SLR radar systems did not reduce the temporal density of the observations, which was approximately 43 scans per hour for these sessions. This is considerably higher than the 15 to 20 scans per hour that is typical for recent IVS 24-hr R1 or R4 geodetic sessions.

The observations covered in this paper took place between December 2014 and January 2017 (see Table 1). For each session the number of observations used in the geodetic analysis can be less than the total number of observations for various reasons. The two main causes are (1) a scan does not produce a valid detection (SNR < 7) and (2) there is too much variation in amplitude among the channels, often due to RFI. See section 6 for a description of the last three columns.

5. Correlation and Broadband Delay Estimation

The Mark6 modules containing the digital data from each station were transported to Haystack for correlation on a distributed FX-type software correlator (Deller et al., 2011). The correlator output is cross-correlation coefficients for each scan (e.g., Whitney et al., 1976). The coefficients are subsequently postprocessed to obtain estimates of the fringe amplitude and phase, group delay, and phase delay rate observables, as well as the difference in charged particle content integrated along the line of sight to a radio source as seen from the two antennas (hereafter dTEC). The following subsections describe the correlator and postprocessing procedures, evaluate uncertainties in the estimated observables, compare dTEC with contemporaneous GPS values, and outline differences between broadband and legacy VLBI processing.

5.1. Correlation

The correlator processes the data from the four VGOS frequency bands simultaneously. This requires reassembling the Mark6 data streams into linux files that are scattered across the eight disks in a Mark6 module.

Besides the recorded data, the correlator needs a wealth of ancillary information to compute an a priori theoretical delay model for each observation. Most of the input information is contained in a VLBI Experiment file, a standard that is currently being expanded to also include broadband-specific features (https://safe.nrao.edu/wiki/bin/view/VLBA/Vex2). The a priori values of most input parameters are known with sufficient accuracy to produce a readily detectable coherent signal without adjustment to those values. This

information has been obtained from various sources for example from the history of VLBI observations for items such as the station and radio source positions, or from recent VLBI or GPS measurements for EOP.

The parameter with the largest uncertainty is usually the UTC time associated with the actual recorded bits. As discussed in section 3.5, the offsets from GPS of the recorded time tags are measured at the stations in real time and applied in the correlation process. However, there are, in addition, instrumental delays at the stations of up to a few microseconds that also impact the relation of the data time tags to UTC. For the sessions reported here the instrumental delays have not been calibrated, but the geodetic results presented (baseline lengths) are not sensitive to these delays.

The goal at the correlator is to reduce the postcorrelation residual delay to less than about 100 ns (see section 5.2.1). Here residual means the difference between the observed value and the a priori value computed in the correlator. This is accomplished by making an initial correlation with a delay search range large enough to include the a priori uncertainty then adjusting the clock of one of the stations by the measured residual.

The output of the VGOS correlation process for a scan is a set of complex correlation coefficients at (typically) 256 different delays spanning four microseconds about the a priori delay value, determined once per second for each of the eight channels in a band, for the four bands, and in two linear polarizations.

5.2. Postcorrelation Analysis

Postprocessing of the correlator output involves finding, in a maximum-likelihood sense, the values of the group delay and phase delay rate that maximize the so-called delay/delay rate resolution function (Rogers, 1970). This fundamental step, for which we used the Haystack Observatory Postprocessing System software package (Whitney et al., 2013), is customarily known in radio interferometry as fringe finding or fringe fitting. VGOS fringe fitting requires multiple runs of the program *fourfit* under different configurations to correct channel phase offsets, synthesize bands, and combine polarizations, ultimately generating a set of calibrated broadband VGOS observables for each scan (Cappallo, 2017).

Calibration involves determining the delay and phase corrections that need to be applied to each frequency channel to adjust for instrumental effects (section 5.2.1). Synthesizing bands entails estimating fringe amplitude, phase, delay, and delay rate at a single fixed value of dTEC (section 5.2.2). Combining polarizations involves coherently adding the output from the four possible linear polarization combinations to yield the broadband VGOS observables (section 5.2.3).

5.2.1. Phasecal Multitone-delay Ambiguity

The multitone delay derived from the phase calibrator phases has an ambiguity of multiples of 200 ns due to the 5-MHz spacing of the tones for which the phases are determined. The path to be measured consists of two parts: from the source of the 5-MHz reference signal to the phasecal generator, and from that point down through the signal chain to the digital backend (Figure 2). The 5-MHz driver for the phase calibrator is common from the maser to the phasecal generator for all bands and polarizations, but the signals from that point to the time-tagged output at the digital backend use different cables and pass through different hardware components for some part of the path for each polarization and for each band. In particular, although the cables for the low band from the output of the dewar to the RDBEs follow essentially the same path as for the high bands, as described above, at GGAO the low-band signal is carried from the antenna to the control room on coaxial cable, while the high band is brought down on optical fiber, giving a difference in delay on the order of 100 ns. At Westford, the low band is carried on a different fiber than the high band, but the delays are comparable.

In order to coherently fit the phases across all four bands in *fourfit*, the phasecal-corrected delays for the bands must agree well enough that the phase change between any pair of the four 512-MHz-wide bands does not exceed half a cycle, corresponding to about 1 ns for the single-band delay. On the other hand, a change of one multitone ambiguity changes the delay by 200 ns, so the ambiguities must be assigned to obtain agreement of the single-band delays among the bands to less than 100 ns. This was effected by examining the single-band delays for the individual bands and adjusting the ambiguities (one for each band) to obtain such agreement. Unless hardware changes are made at a station that result in a significant path delay change (tens of nanoseconds), the values used for the ambiguities will not require modification. This might occur if, for example, the 5-MHz coaxial cable at GGAO were replaced by optical fiber.

The initial values for the sampler delays at each station were set to approximate the expected delay due to the cable configuration. Because both polarizations traverse the same path to within a few meters, the sampler delay values for both polarizations are set the same for each band. For GGAO the values for band A were adjusted, relative to bands B–D, to account for the coax-fiber delay difference.

5.2.2. The Effect of dTEC on Broadband Synthesis

The method for determining dTEC is to successively estimate the observables—fringe amplitude, phase, delay, and delay rate—at a grid of fixed values of dTEC that span a specified range. The dTEC values obtained on this relatively short (i.e., ~600 km) baseline were found to span ±12 TECU (1 TECU = 10^{16} el m^{-2}), but dTEC values of up to 100 TECU can be expected on longer baselines. The search is done in three steps: first, *fourfit* is run on a coarse grid of dTEC values; next, a smoothing function (a half-cycle of a cosine function with a half-width of about 4 TECU) is convolved with the estimated amplitudes at the grid points; then, *fourfit* is run on a finer grid that is centered on the dTEC value that gave the largest smoothed amplitude. The dTEC value corresponding to the actual maximum amplitude is found by interpolation within the three dTEC values that gave the highest amplitudes in the fine search. This dTEC value, which likely was not used for one of the search values, is then held fixed in a final run of *fourfit* to estimate the observables.

For this short baseline, we used a coarse grid search of ±88 TECU in steps of 4 TECU followed by a finer grid search of ±6 TECU at a spacing of 0.4 TECU and found that the process converged.

There is a high correlation between the estimated delay (phase proportional to frequency) and the dispersion term as parameterized by dTEC (phase inversely proportional to frequency), with a typical value for the correlation greater than 0.95. The evaluation of the uncertainties of these two parameters is described in section 5.4.

5.2.3. Combining Polarizations

The broadband group delay and phase for a scan are obtained by calculating in *fourfit* for each accumulation period a linear combination of the four complex polarization correlation coefficients, HH, VV, HV, and VH, for all four frequency bands:

$$I = (H_a^* H_b + V_a^* V_b)\cos\Delta + (H_a^* V_b - V_a^* H_b)\sin\Delta, \tag{1}$$

where I is the total intensity (also known as Stokes parameter S_0), a and b identify each antenna, * denotes complex conjugate, and Δ is the difference of the parallactic angles between the two antennas (Cappallo, 2012). In actuality, the linear combination as defined in equation (1) is a pseudo-Stokes I parameter, which differs from the proper Stokes definition in that it is dimensionless, rather than expressed in Janskys, and that the magnitudes are set to unity for the complex system gains for both polarizations at a station.

From equation (1), one can see that for a parallactic angle difference of 0°, the polarizations of the two feeds are aligned so that HH and VV are the strongest products, while for a difference of 90°, VH and HV are strongest. Differential Faraday rotation also contributes to Δ, but the magnitude, while not known, is less than 10° at VGOS frequencies and is ignored by *fourfit*.

However, in order to combine these data coherently, any differences of delay and phase between the two polarizations that were not corrected by the phasecal approach must be removed. Such differences are expected to occur largely ahead of the injection of the phasecal signals in the RF signal path (Figure 2) and can be determined most readily and accurately from the observations. They are calculated as linear combinations of the delays and phases and are obtained by running *fourfit* to combine all four bands for each of the four cross-polarization products. Since only the differences between the polarizations are required, the phase and delay offsets associated with the horizontal polarization are set to 0 without loss of generality. For example, the group delay offset of the Westford vertical polarization, wV, from the horizontal polarization, wH, can be obtained relative to the GGAO horizontal polarization, gH, from the difference of the group delays, gHwH-gHwV, to give wV-wH, where gHwH is the cross correlation of the horizontal polarizations for the two stations. The four combinations HH, HV, VH, and VV provide the H-V differences for both antennas. In practice, all of the scans with SNRs greater than about 30 for all polarization combinations are used to determine the offsets. The same procedure provides the H-V phase differences for both stations. The average differences over a session for group delay and phase for the two stations are incorporated in the *fourfit* calculation of the pseudo-Stokes I.

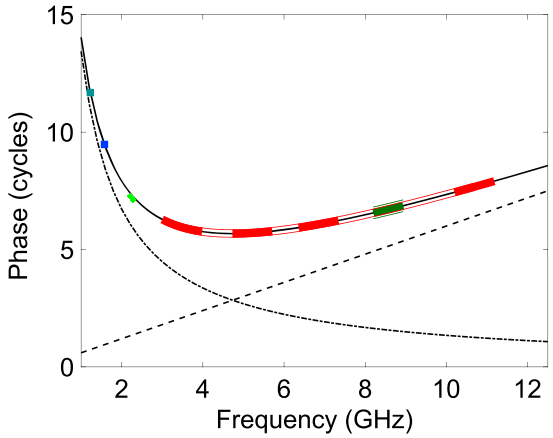

Figure 6. Calculation of total phase (solid line, top) versus frequency through the GPS (blue), legacy VLBI (light and dark green for S and X), and VGOS (red) observing bands, obtained as the sum of a delay of 600 ps (dashed line) and a difference in TEC between lines of sight to the two antennas (dTEC) of 10 TECU (dash-dot line). The bands are GPS L1 and L2 at approximately 1.2 and 1.6 GHz, legacy VLBI S- and X-bands at 2.2 and 8.4 GHz, and VGOS 1-GHz bands A–D centered on 3.5, 5.5, 6.5, and 10.5 GHz, respectively. The values chosen for delay and dTEC are arbitrary. The widths of the bands are shown to scale. GPS = Global Positioning System; VLBI = very long baseline interferometry; VGOS = VLBI Global Observing System; TEC = total electron content.

5.3. Uncertainty of the Broadband Delay Observable

The theoretical uncertainty for the group delay, σ_τ, as calculated in *fourfit*, depends on the SNR and the root-mean-square of the channel frequencies (e.g., Thompson et al., 2017):

$$\sigma_\tau = \frac{1}{2\,\pi\,\mathrm{SNR}\sqrt{<(\nu_i - \bar{\nu})^2>}}, \tag{2}$$

where ν_i is the center frequency of each channel in all bands, $\bar{\nu}$ is the mean of the center frequencies, and $< >$ denotes average. SNR is the product of the amplitude from *fourfit*, the total number of samples recorded, and a factor that accounts for 2-bit digitization and the DiFX bandpass shape. The broadband group delay utilizes the connected phases over a spanned frequency range of about 7.7 GHz, while the legacy VLBI delay is determined from phases spanning only 0.7 GHz at X-band; the S-band group delay is used only for the dispersion correction.

Equation (2) is accurate when only the group delay, delay rate, and phase are estimated, such as in the case of the *narrow* bandwidth (i.e., 730 MHz at X-band) of legacy VLBI. The expression is, however, not complete for the ~7-GHz bandwidth of the VGOS observable because it ignores dTEC, for which the phase follows a ν^{-1} dependence (Figure 6). Ignoring the effect of dTEC on the estimated delay over the VGOS broadband results in a group delay that is biased and a group delay uncertainty that is underestimated.

When dTEC is estimated, the uncertainty of the group delay is larger than would be calculated by equation (2) by a factor of approximately 2.6 due to the inclusion of the additional parameter since the group delay and dTEC are highly correlated (Cappallo, 2015). The program *fourfit* has therefore been enhanced to incorporate the correlations among the group delay, delay rate, dTEC, and phase in calculating the group delay uncertainty. The resulting uncertainty is reported for the broadband delay that is used for the geodetic estimation.

The performance goals of VGOS are to increase the temporal scan density relative to legacy VLBI while achieving significantly better group delay precision (Petrachenko et al., 2009). The increase in density is effectively accomplished by using fast antennas and reducing the scan duration. The improved delay uncertainty is obtained through the increased data acquisition record rate and a much wider spanned bandwidth.

Two schedules were generated to illustrate the anticipated improvements, one for a pair of legacy-type antennas and one for a pair of VGOS antennas. The antenna locations were Westford and GGAO. For the legacy schedule the antenna properties were characteristic of the 20-m antennas at Wettzell, Kokee, and Ny Alesund

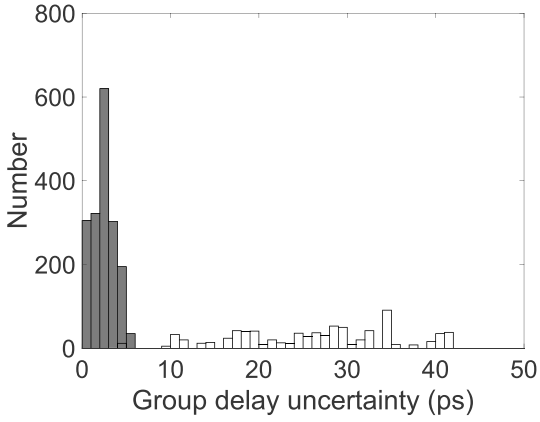

Figure 7. Histograms of the distributions of the calculated group delay uncertainties for a 24-hr schedule for two VGOS antennas (1,780 scans, dark) and two legacy VLBI antennas (801 scans, clear).

Table 2
Comparison of Broadband and Legacy Performance for a 0.25 Jy Source

System	SEFD	Recorded BW (GHz)	SNR	Scan length (s)	Delay uncertainty (ps)	dTEC uncertainty (TECU)
S/X	1,500	0.080[a]	20[a]	105.2	31.1	12.2
Broadband	2,500	2.048	20	11.4	8.0	0.2

[a]The bandwidth used is that of X-band only since the S-band delay is used only to correct for the dispersion. The same SNR is used for both X and S in the delay uncertainty calculation. SEFD = system equivalent flux density; BW = bandwidth; SNR = signal-to-noise ratio; TECU = total electron content unit.

(SEFD 1,500 Jy at both S and X; slew rates 2.5°/s in both axes), while the VGOS antennas were given the VGOS requirement values (SEFD 2,500 Jy in all bands; slew rates 12°/s in azimuth and 5°/s) in elevation). The data rates were 512 Mbps for legacy and 8 Gbps for VGOS. For both systems the minimum SNR was set to 15 and the minimum scan length to 15 s. A summary of the generated schedule gave for each scan the duration, the expected correlated flux densities in S- and X-bands (which were averaged for VGOS), and the expected SNR in both bands. From these and the antenna properties the delay uncertainties were calculated.

Figure 7 shows the group delay uncertainty distributions for the two schedules. The figure illustrates both the significantly smaller delay uncertainties and the greater number of observations for the VGOS systems under identical scheduling conditions.

The benefits of the broadband system are further displayed in Table 2, which gives the scan duration and delay uncertainty for a radio source with a correlated flux density of 0.25 Jy, which would be among the weakest to be observed. The scan length for the VGOS system is approximately one tenth that of the legacy scan, and the delay uncertainty is one quarter.

5.4. Precision of dTEC Estimation

An important improvement of the broadband approach versus legacy VLBI is the better precision of the dTEC estimate, hence improved calibration of the delay observable for dispersive effects. While the former involves four widely distributed bands, the latter is a dual-frequency approach conceptually similar to the GPS. The improved precision for the broadband dTEC comes primarily from estimating only one additional parameter for the dispersion term across the connected phases of all four bands compared to estimating the two separate group delays for S-band and X-band and differencing them (see Figure 6). The dTEC uncertainty for S/X is determined almost entirely by the S-band group delay uncertainty, which is approximately 50 times larger than the undispersed broadband group delay uncertainty.

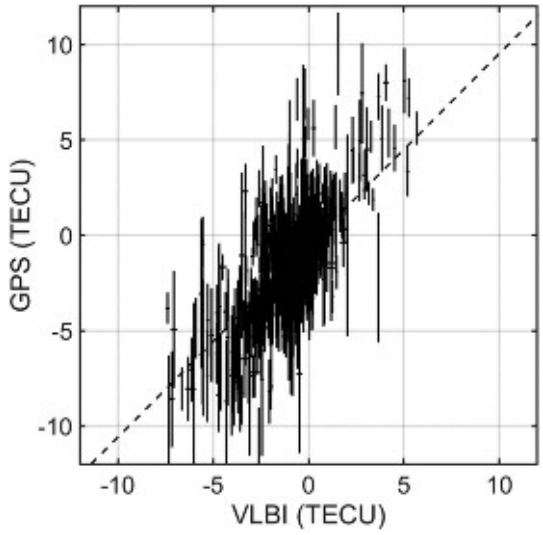

Figure 8. Scatter plot of dTEC between Westford and GGAO as measured by VGOS (horizontal error bar) and calculated for GPS (vertical error bar). The VGOS data are for session V15342 (Table 1). The dashed line is a linear fit and shows intertechnique consistency at the 1-TECU level. VGOS = VLBI Global Observing System; TECU = total electron content unit; GPS = Global Positioning System.

Figure 8 shows the dTEC estimates computed for GPS versus the value for the same scan for VGOS. The GPS estimates are formed for the lines of sight, at the time of each scan, corresponding to the same antenna locations. The line-of-sight direction for total electron content (TEC) measurements from a GPS antenna collocated with a VLBI system are not likely to coincide with the directions of the VLBI radio sources at the specific time of the observation because of the small number of GPS satellites. Therefore, TEC data for the comparison were obtained from the Madrigal database (Rideout & Coster, 2006).

The Madrigal database contains zenith TEC values derived from the global GPS network on an Earth-surface 1° by 1° grid with a temporal resolution of 5 minutes. For both stations of each VLBI observation the latitude and longitude of the pierce point of the signal from the radio source through the ionosphere to the antenna was calculated for a height above the surface of 350 km. The Madrigal database was searched for the vertical TEC values at the two pierce points. These values were then converted to slant-path TEC using the mapping function of Rideout and Coster (2006). The best fit, in a linear weighted-least-squares sense, of the GPS values at the VGOS values yields a scale (slope) of 1.01 ± 0.04 and a dTEC bias of GPS relative to VLBI of -0.5 ± 0.1 TECU (Figure 8), thus showing consistency

at the level of 1 TECU, or better, over a range of about 10 TECU. (Investigation of dTEC precision over longer baselines, hence larger dTEC variations, remains as future work.)

5.5. Correlation and Processing Differences Between VGOS Broadband and Legacy VLBI

VGOS broadband differs from legacy VLBI in several significant areas of correlation and postcorrelation processing. These areas are polarization correlation, combining the two independent polarizations, and dTEC estimation.

Most legacy antennas receive only right-circular polarization, so only one correlation product is needed. A fundamental element of the broadband concept is the use of both polarizations, one benefit of which is to improve the sensitivity of the systems. In order to cover the large frequency range with a single feed, current technology can support only linearly polarized feeds for the antennas that meet the requirements for sensitivity and speed. However, because the global distribution of the VGOS network results in a wide range of differences in parallactic angle among the antennas, it is necessary to correlate all polarization products—HH, HV, VH, and VV—and combine them coherently to recover the full sensitivity of the antenna pair.

The combination of all bands and polarizations requires that the delays and phases (at a common reference frequency) of the eight band-polarization correlations agree sufficiently well, prior to combining, that coherence is not reduced. This is achieved by using phasecal multitone delays rather than the single tone phase correction generally used for legacy VLBI, allowing for different sampler delays for the different bands, incorporating the delay and phase differences between polarizations, and estimating simultaneously the phase dispersion term with the group delay. The last is a markedly different approach from legacy VLBI, whereby the dispersion term is calculated from the group delays determined separately for the two observing bands (Figure 6).

6. Geodetic Analysis, Results, and Discussion

We used a standard geodetic VLBI strategy to process the VGOS data using *nuSolve*, a new interactive preprocessor of the *solve* software package (Bolotin et al., 2016). The VGOS data consist of broadband delays (equation (1)) for the baseline between Westford and GGAO obtained approximately once every 70 s and from about 50 radio sources for the 24-hr-long sessions (Table 1). Each observing session was processed separately. For each session we estimated the clock model at GGAO relative to Westford as the reference, the atmosphere wet zenith delays and gradients at both sites, and the length of the baseline. The position and clock of Westford were kept fixed. The positions of the radio sources and consistent Earth rotation parameters were obtained from the IVS and were not estimated in our analysis.

The clock parameterization of GGAO was modeled as a quadratic term plus 20-min piecewise-linear segments with an a priori sigma for the rate terms of 72 ps/hr. Atmospheric delays were modeled as the sum of 15-min piecewise-linear zenith delay segments and 1-hr piecewise-linear gradient segments, with intentionally very weak constraints for the rate terms of, respectively, 12 mm/h and 3×10^8 mm/h, which are the default values in *nuSolve* (Bolotin et al., 2016).

Table 1 shows performance metrics such as session length, number of observations, and WRMS of the postfit delay residuals. The WRMS given in column 6 is obtained using as data weights in the *nuSolve* estimator the formal uncertainties of the delay observables, which are typically a few ps (Figure 7). The corresponding chi-squared per degree of freedom, χ^2_ν, of all sessions (not shown in the table) is between approximately 25 and 150, indicating that the model parameterization is either incomplete or incorrect or that the delay uncertainties are underestimated, or both. Column 7 gives the amount of delay noise that was added in quadrature to the observation uncertainties to make $\chi^2_\nu = 1$, and column 8 gives the WRMS of the resulting reweighted solutions.

For example, for the 24-hr session on 8 December 2015 (session V15342) the group delay uncertainties are less than 1 ps for 41% of the scans and less than 4 ps for 77% of the scans, and the median uncertainty is 1.8 ps. These values are representative of all of the sessions, even with the prototype systems. The WRMS of the postfit delay residuals after reweighting is 9.4 ps, which is slightly less than the median WRMS of all sessions of 11.1 ps. The additive delay uncertainty for reweighting is 10.0 ps, which dominates the per-scan uncertainty. For comparison, the typical WRMS postfit delay residual for the weekly R1 and R4 observing sessions of the IVS is about 40 ps.

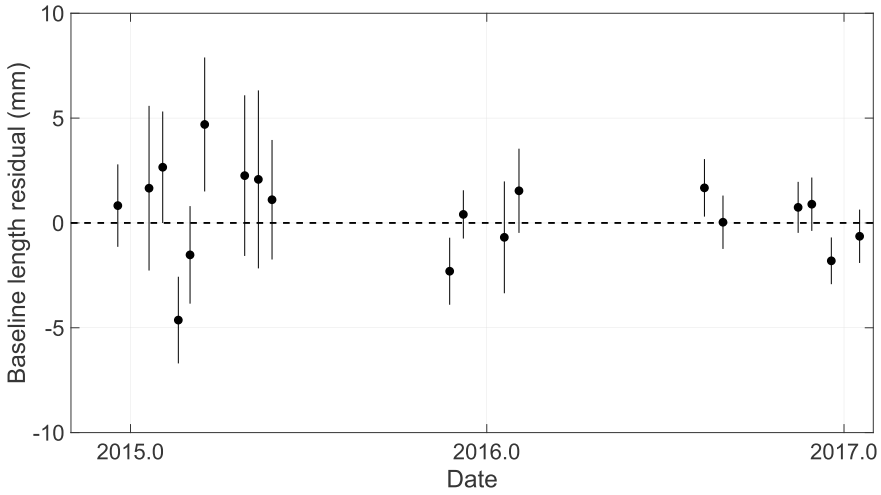

Figure 9. Time series of the residuals to the weighted mean of the length estimates of the GGAO-Westford baseline for the sessions listed in Table 1. Unmodeled noise of 1.1 mm has been added quadratically to each length uncertainty to make $\chi^2_\nu = 1$ over all sessions, resulting in a WRMS residual of 1.6 mm.

Figure 9 shows the residuals to the weighted mean of the estimated lengths (600,796,027.7 mm) of the baseline between Westford and GGAO for the 19 sessions from 19 December 2014 to 17 January 2017. In this early stage of VGOS data validation, we have focused on the time series of baseline lengths and not on the components of site position because the former is invariant to rotations, hence insensitive to errors in the assumed values for Earth rotation parameters and reference frame realizations.

For the 19 sessions the WRMS residual of the reweighted lengths is 1.2 mm with a χ^2_ν of 4.7. The χ^2_ν can be reduced to 1.0, resulting in a length WRMS of 1.6 mm, if an unmodeled noise of 1.1 mm is added quadratically to each length uncertainty. There are several possible sources of this noise, among which are unmodeled clock and atmosphere delay variations, unmodeled radio source structure, and errors in the cable delay corrections. However, for the first nine sessions the larger uncertainties and scatter are due primarily to their shorter duration (see Table 1).

These results incorporate delay corrections (relative to the beginning of each session) for both stations for the cable carrying the 5-MHz reference frequency signal from the maser to the phasecal generator (see section 3.4.2). To illustrate the effect of cable delays on the geodetic estimates, all sessions were processed omitting any of the cable delay corrections. The corrected lengths differed from the uncorrected lengths by −6 to +12 mm, and for 14 of the 19 sessions the deviation from the mean was reduced by making the corrections. Additionally, the WRMS of the postfit delay residuals was reduced for the majority of sessions by the inclusion of the cable delay. Although the proxy approach, which was used for all sessions for GGAO and for the first eleven for Westford, is an improvement over having no calibration, a CDMS measurement is expected to be a better correction than the proxy value, primarily because it is a measurement of only the cable delay and is not contaminated by variations in the signal chain components. It is thus seen as necessary for achieving the goal of 1-mm length repeatability that CDMS corrections be used at all VGOS stations.

We note that the few millimeter repeatability is for a short ~600-km baseline for which the degree of error cancelation is expected to be larger than for long baselines. For example, the length of a short baseline is far more sensitive to errors in the horizontal components of site position than in the vertical. This is advantageous because vertical errors are typically larger than horizontal errors. For this baseline, an error in the vertical position of one antenna has an effect on baseline length of less than 0.05 mm per mm of vertical error, while a horizontal position error goes into the length directly as the projection of the error on the direction to the other antenna. Thus, the effect on baseline length of errors that are elevation dependent (i.e., contributing largely to the local vertical component of station position) is negligible for this baseline.

On the other hand, azimuth-dependent errors (i.e., largely horizontal), due, for example, to changes in the cable carrying the 5-MHz reference frequency signal to the phase calibrator, have a detectable effect on

baseline length estimates, the magnitude depending on both the size of the delay error and the form of the azimuthal dependence. To complicate matters, any azimuth dependence of the delay errors will also have an effect on the estimated atmosphere gradients because of the similar dependence on azimuth. Therefore, it is desirable to remove any azimuth-dependent delay errors in order to improve estimation of the gradients and thus of the antenna position. Ultimately, CDMS corrections that accurately correct both elevation- and azimuth-dependent cable delay errors will be necessary at all VGOS stations.

7. Progress Toward the VGOS Objectives

This study demonstrates compliance with three of the four recommendations to establish an operational, high-accuracy VGOS network (Niell et al., 2006; Petrachenko et al., 2009). The specific recommendations addressed are the design of a new observing system based on small, agile antennas coupled with broadband receivers, the recording and transfer of data using a combination of high data rate (8-Gbps) disk modules and high-speed networks, and the processing of interferometric data using a software correlator with broadband capabilities. As for the fourth recommendation—automate and streamline the complete data-analysis pipeline—various components, such as developing multiband and dual-polarization processing capabilities, have been implemented for the single-baseline VGOS prototype, but a fully automated end-to-end data processing of a large VGOS network remains a future challenge.

The study also addressed three of the four proposed strategies that resulted from the VGOS simulation studies to achieve 1-mm site position accuracy from 24-hr observations (Petrachenko et al., 2009), namely, to reduce the average source-switching interval, to decrease the random component of the delay error, and to minimize the susceptibility to RFI. In the current study, we observed between 45 and 50 observations per hour, a factor of 2–4 increase from legacy VLBI observations. The reduction of delay error is quite significant (Figure 7), achieving a median delay measurement uncertainty of only a few picoseconds. Reduction of RFI effects is accomplished through effective observing frequency selection to avoid known sources of RFI and by splitting the RF signal downlink into high and low bands to mitigate the impact on fiber links. The fourth strategy component, which is the reduction of systematic errors such as radio source structure, antenna deformation, and instrumental drifts, will be addressed as more data become available with the rollout of the VGOS network.

While the primary goal of this study was to develop the procedures required for successful VGOS operations, including data acquisition and the processing from scheduling through geodetic analysis, a large number of engineering innovations have been introduced and implemented, both in hardware and software, that will propel VGOS into the future. Examples include the new digital phasecal generator, the up-down converter, digital backend, Mark6 high-data-rate recorder, simultaneous estimation of delay and dispersion parameters, and the combination of multiple bands and dual polarizations to create the pseudo-Stokes-I amplitude and delay.

8. Conclusions and Future Work

We have developed two prototype VGOS systems at Westford and GGAO and have operated this 600-km-long VGOS baseline since December 2014. The estimated baseline length between Westford and GGAO from 19 observing sessions over a 2-year period yielded a WRMS deviation of length residuals about the weighted mean of 1.6 mm. These results demonstrate the feasibility of the VLBI2010 broadband delay concept (Niell et al., 2006). A few fully compliant VGOS antenna systems have since been deployed that will pave the way for global, high-accuracy VGOS observations.

The main conclusion of the VLBI2010 studies was that the primary limitation to station position accuracy was the deleterious effect of the atmosphere, which could be reduced by faster atmospheric sampling through increased number of scans per unit time. The minimum scan length of the sessions presented here was set to 30 s, yielding about 50 scans per hour. The goal is at least two scans per minute, which should be possible with the fast slew rates of the new VGOS antennas. It remains for further analysis of these and ongoing VGOS observations to assess the accuracy limitation imposed by the atmosphere delay variability.

Achieving such high-rate VGOS observations will also require improvements to the scheduling program, radio source catalogs, and postcorrelation analysis. In particular, source catalogs should be revisited to include accurate information on correlated flux density for each source, baseline, and frequency band to guarantee robust detections. This information will also be important for choosing the most compact radio sources among those

that can be observed. For the relatively short Westford-GGAO baseline, source structure does not seem to have had any significant impact on the accuracy of length estimates, as judged by the consistency of the post-fit delay residuals among the sources. However, as VGOS baselines become longer and sources are resolved, their extended structures will have an accuracy impact if left uncorrected. Besides the obvious approach of not observing *problem* sources, one could alternatively look into mitigating the effect by correcting for the structure contribution by using VLBI imaging techniques (e.g., Charlot, 1990; Xu et al., 2016).

An area that also deserves special attention is the effect of uncalibrated instrumental delays and phases. The most significant problem as of this writing is the lack of a CDMS at some of the new and upcoming VGOS antennas. The significance of such an omission, which can be at the several millimeter level, was demonstrated in section 3.4.2.

It has long been recognized that the major operational hurdle for VGOS is the transfer of the observed data to the correlators (Petrachenko et al., 2009). For this study, the data of only a few of the short 1-hr sessions were transferred from GGAO to the Haystack correlator via the Internet. For the 24-hr sessions, prompt shipment of the data modules proved to be faster and more efficient than an electronic transfer largely due to the limited network bandwidth. The VGOS vision is for continuous observations with a network of a few tens of stations globally distributed. Under the projected improvements in network bandwidth, the electronic transfer of VGOS data remains a significant challenge.

Acknowledgments
We would like to thank John Labrecque and Chopo Ma, NASA/Goddard Space Flight Center (GSFC), for supporting the development of the original broadband proof-of-concept systems for MV-3 and the two VGOS stations at GGAO and Westford. We acknowledge support from Stephen Merkowitz, GSFC, and many other colleagues involved in the NASA Space Geodesy Project (SGP). We appreciate the efforts of the Editors and three anonymous reviewers whose constructive suggestions significantly improved the paper. We also thank Peter Bolis, John Byford, and Don Sousa, MIT Haystack Observatory, for their valuable contributions through procurement, construction, and maintenance of the GGAO antenna and the broadband frontends of both GGAO and Westford and for shipping; Christopher Beaudoin for his engineering contributions to the VGOS efforts while at MIT Haystack Observatory; Katie Pazamickas and Jay Redmond, Peraton, for operations support at GGAO; Carlos Mulero, participant in the NSF-funded Research Experiences for Undergraduates (REU) program at Haystack in 2014, for software leading to the dTEC comparison; Anthea Coster, Bill Rideout, and Juha Vierinen, Haystack, for discussions of TEC measurement by GPS; Sandy Weinreb and Ahmed Akgiray, Caltech, for advice on dewar construction and for accommodating multiple QRFH designs, including a special design for Westford; Nancy Kotary, Haystack, for her graphics mastery. The work by MIT Haystack Observatory was supported under NASA contracts NNG10HP00C and NNG15HZ35C. The work by NVI, Inc. was supported under NASA contract NNG17HS00C. B. Petrachenko thanks Natural Resources Canada for support. The databases from which the baseline lengths were calculated are available in the CDDIS archives.

References

Abdalati, A., Gail, W. B., & Busalacchi, A. J. Jr. (2018). *Thriving on our changing planet: A decadal strategy for Earth observation from space*, National Academies of Sciences, Engineering, and Medicine. Washington, DC: The National Academies Press. https://doi.org/10.17226/24938

Akgiray, A., Weinreb, S., Imbriale, W. A., & Beaudoin, C. (2013). Circular quadruple-ridged flared horn achieving near-constant beamwidth over multioctave bandwidth: Design and measurements. *IEEE Transactions on Antennas and Propagation*, *61*(3), 1099–1108. https://doi.org/10.1109/TAP.2012.2229953

Altamimi, Z., Rebischung, P., Métivier, L., & Collilieux, X. (2016). ITRF2014: A new release of the International Terrestrial Reference Frame modeling non-linear station motions. *Journal of Geophysical Research: Solid Earth*, *121*, 6109–6131. https://doi.org/10.1002/2016JB013098

Bare, C., Clark, B. G., Kellermann, K. I., Cohen, M. H., & Jauncey, D. L. (1967). Interferometer experiment with independent local oscillators. *Science*, *157*, 189–191. https://doi.org/10.1126/science.157.3785.189

Bolotin, S., Baver, K., Gipson, J., Gordon, D., & MacMillan, D. (2016). Transition to the vgosDb format. In *9th IVS General Meeting, NASA/CP-2016-219016* (pp. 222–224).

Broten, N. W., Legg, T. H., Locke, J. L., McLeish, C. W., Richards, R. S., Chisholm, R. M., et al. (1967). Long base line interferometry: A new technique. *Science*, *156*, 1592–1593. https://doi.org/10.1126/science.156.3782.1592

Cappallo, R. (2011). Multitone phasecal mode in fourfit (Tech. rep.): MIT Haystack Observatory. https://www.haystack.mit.edu/tech/vlbi/hops/multitone_phasecal.pdf

Cappallo, R. (2012). Memo on recent mods (v3.7) (Tech. rep.): MIT Haystack Observatory. https://www.haystack.mit.edu/tech/vlbi/hops/fourfit_3.7_features.pdf

Cappallo, R. (2015). Covariance analysis of the simultaneous fit of group delay and dTEC in fourfit (Tech. rep.): MIT Haystack Observatory. https://www.haystack.mit.edu/tech/vlbi/hops/simul_ion_fit.pdf

Cappallo, R. (2017). Fourfit user's manual (Tech. rep.), MIT Haystack Observatory. https://www.haystack.mit.edu/tech/vlbi/hops/fourfit_users_manual.pdf

Carter, W. E., Robertson, D. S., Pettey, J. E., Tapley, B. D., Schutz, B. E., Eanes, R. J., & Lufeng, M. (1984). Variations in the rotation of the Earth. *Science*, *224*(4652), 957–961. https://doi.org/10.1126/science.224.4652.957

Charlot, P. (1990). Radio-source structure in astrometric and geodetic very long baseline interferometry. *The Astronomical Journal*, *99*, 1309–1326. https://doi.org/10.1086/115419

Davis, J. L. (2010). *Precise geodetic infrastructure: National requirements for a shared resource*, National Academies of Sciences, Engineering, and Medicine. Washington, DC: The National Academies Press.

Davis, J. L., Kellogg, L. H., Arrowsmith, J. R., Buffett, B. A., Constable, C. G., Donnellan, A., et al. (2016). Challenges and Opportunities for Research in ESI (CORE) (Tech. rep.). Arlington, Virginia: Report from the NASA Earth Surface and Interior (ESI) Focus Area Workshop November 2–5, 2015. https://smd-prod.s3.amazonaws.com/science-green/s3fs-public/atoms/files/CORE2016.pdf

Deller, A. T., Brisken, W. F., Phillips, C. J., Morgan, J., Alef, W., Cappallo, R., et al. (2011). DiFX-2: A more flexible, efficient, robust, and powerful software correlator. *Publications of the Astronomical Society of the Pacific*, *123*(901), 275.

Gipson, J. (2012). Sked: VLBI scheduling software (Tech. rep.). Greenbelt, MD: NVI/Goddard Space Flight Center. https://vlbi.gsfc.nasa.gov/files_user_manuals/sked/SkedManual_v2016Dec09.pdf

Gipson, J., & Baver, K. (2016). Improvement of the IVS-INT01 sessions by source selection: Development and evaluation of the maximal source strategy. *Journal of Geodesy*, *90*(3), 287–303. https://doi.org/10.1007/s00190-015-0873-6

Gold, T. (1967). Radio method for the precise measurement of the rotation period of the Earth. *Science*, *157*(3786), 302–304. https://doi.org/10.1126/science.157.3786.302

Herring, T. A., Davis, J. L., & Shapiro, I. I. (1990). Geodesy by radio interferometry: The application of Kalman filtering to the analysis of very long baseline interferometry data. *Journal of Geophysical Research*, *95*(B8), 12,561–12,581. https://doi.org/10.1029/JB095iB08p12561

Herring, T. A., Shapiro, I. I., Clark, T. A., Ma, C., Ryan, J. W., Schupler, B. R., et al. (1986). Geodesy by radio interferometry: Evidence for contemporary plate motion. *Journal of Geophysical Research*, *91*(B8), 8341–8347. https://doi.org/10.1029/JB091iB08p08341

Hinteregger, H. F., Shapiro, I. I., Robertson, D. S., Knight, C. A., Ergas, R. A., Whitney, A. R., et al. (1972). Precision geodesy via radio interferometry. *Science*, *178*(4059), 396–398. https://doi.org/10.1126/science.178.4059.396

Imbriale, W. A., Weinreb, S., & Mani, H. (2007). Design of a wideband radio telescope. In *2007 IEEE Aerospace Conference*, pp. 1–12. https://doi.org/10.1109/AERO.2007.352858

Kellermann, K. I., & Moran, J. M. (2001). The development of high-resolution imaging in radio astronomy. *Annual Review of Astronomy and Astrophysics*, *39*(1), 457–509. https://doi.org/10.1146/annurev.astro.39.1.457

Moran, J., Crowther, P., Burke, B., Barrett, A., Rogers, A., Ball, J., et al. (1967). Spectral line interferometry with independent time standards at stations separated by 845 kilometers. *Science*, *157*(3789), 676–677. https://doi.org/10.1126/science.157.3789.676

Niell, A., Bark, M., Beaudoin, C., Brisken, W., Frej, H. B., Doeleman, S., et al. (2010). RDBE development and progress. In *IVS 2010 General Meeting Proceedings*, pp. 396–399. NASA/CP-2010-215864.

Niell, A. E., Whitney, A. R., Petrachenko, B., Schluter, W., Vandenberg, N. R., Hase, H., et al. (2006). VLBI2010: Current and future requirements for geodetic VLBI systems (WG3—final report). In *2005 IVS Annual Report NASA/TP-2006-214136*. International VLBI Service for Geodesy and Astrometry (IVS).

Pany, A., Böhm, J., MacMillan, D., Schuh, H., Nilsson, T., & Wresnik, J. (2011). Monte Carlo simulations of the impact of troposphere, clock and measurement errors on the repeatability of VLBI positions. *Journal of Geodesy*, *85*(1), 39–50.

Petit, G., & Luzum, B. (2010a). IERS conventions (2010). ISBN 3-89888-989-6, Verlag des Bundesamts für Kartographie und Geodäsie Frankfurt am Main, IERS Technical Note No. 36, 179 pp.

Petit, G., & Luzum, B. (Eds.) (2010b). *IERS conventions, 179 pp Edited by* Petit, G., & Luzum, B.Frankfurt am Main: Verlag des Bundesamts für Kartographie und Geodäsie.

Petrachenko, B. (2008). Performance of broadband delay (BBD) sequences (Tech. Rep.): IVS-2008-005v01, IVS Technical Memorandum. https://ivscc.gsfc.nasa.gov/publications/memos/ivs-2008-005v01.pdf

Petrachenko, B., Niell, A., Behrend, D., Corey, B., Bohm, J., Charlot, P., et al. (2009). Design aspects of the VLBI2010 system. Progress report of the VLBI2010 committee (Tech. Rep.): NASA/TM-2009-214180, NASA Technical Memorandum. https://ivscc.gsfc.nasa.nasa.gov/publications/misc/TM-2009-214180.pdf

Rideout, W., & Coster, A. (2006). Automated GPS processing for global total electron content data. *GPS Solutions*, *10*(3), 219–228.

Robertson, D. S. (1991). Geophysical applications of very-long-baseline interferometry. *Reviews of Modern Physics*, *63*, 899–918. https://doi.org/10.1103/RevModPhys.63.899

Robertson, D. S., Carter, W. E., Eanes, R. J., Schutz, B. E., Tapley, B. D., King, R. W., et al. (1983). Comparison of Earth rotation as inferred from radio interferometric, laser ranging, and astrometric observations. *Nature*, *302*(5908), 509–511.

Rogers, A. E. E. (1970). Very long baseline interferometry with large effective bandwidth for phase-delay measurements. *Radio Science*, *5*(10), 1239–1247. https://doi.org/10.1029/RS005i010p01239

Rogers, A. E. E. (2006). 1024/2048 MHz clock synthesizer for DBE (Tech. rep.): MIT Haystack Observatory. https://www.haystack.mit.edu/tech/vlbi/mark5/mark5_memos/042.pdf

Rogers, A. E. E. (2008). Modification to NASA/Honeywell pcal for 5 MHz repetition rate (Tech. rep.): MIT Haystack Observatory.https://www.haystack.mit.edu/geo/vlbi_td/BB/017.pdf

Rogers, A. E. E. (2009). Phasecal processing (Tech. rep.): MIT Haystack Observatory. https://www.haystack.mit.edu/geo/vlbi_td/BB/026.pdf

Rogers, A. E. E. (2015). Tests of new digital phase calibrator (Tech. rep.): MIT Haystack Observatory. https://www.haystack.mit.edu/geo/vlbi_td/BB/023.pdf

Rogers, A. E. E., Cappallo, R. J., Hinteregger, H. F., Levine, J. I., Nesman, E. F., Webber, J. C., et al. (1983). Very-long-baseline radio interferometry: The Mark III system for geodesy, astrometry, and aperture synthesis. *Science*, *219*(4580), 51–54. https://doi.org/10.1126/science.219.4580.51

Schuh, H., & Behrend, D. (2012). VLBI: A fascinating technique for geodesy and astrometry. *Journal of Geodynamics*, *61*, 68–80. https://doi.org/10.1016/j.jog.2012.07.007

Seidelmann, P. K., & Kovalevsky, J. (2002). Application of the new concepts and definitions (ICRS, CIP and CEO) in fundamental astronomy. *Astronomy & Astrophysics*, *392*, 341–351. https://doi.org/10.1051/0004-6361:20020931

Sovers, O. J., Fanselow, J. L., & Jacobs, C. S. (1998). Astrometry and geodesy with radio interferometry: Experiments, models, results. *Reviews of Modern Physics*, *70*, 1393–1454. https://doi.org/10.1103/RevModPhys.70.1393

Sun, J., Böhm, J., Nilsson, T., Krásná, H., Böhm, S., & Schuh, H. (2014). New VLBI2010 scheduling strategies and implications on the terrestrial reference frames. *Journal of Geodesy*, *88*(5), 449–461. https://doi.org/10.1007/s00190-014-0697-9

Thompson, A. R., Moran, J. M., & Swenson, G. W. Jr. (2017). *Interferometry and synthesis in radio astronomy* (3rd ed.). Cham, Switzerland: Springer. https://doi.org/10.1007/978-3-319-44431-4

Welch, J., Backer, D., Blitz, L., Bock, D., Bower, G. C., Cheng, C., et al. (2009). The Allen Telescope Array: The first widefield, panchromatic, snapshot radio camera for radio astronomy and SETI. *Proceedings of the IEEE*, *97*(8), 1438–1447. https://doi.org/10.1109/JPROC.2009.2017103

Whitney, A. R., Beaudoin, C. J., Cappallo, R. J., Corey, B. E., Crew, G. B., Doeleman, S. S., et al. (2013). Demonstration of a 16 Gbps per station broadband-RF VLBI system. *Publications of the Astronomical Society of the Pacific*, *125*(924), 196.

Whitney, A., Kettenis, M., Phillips, C., & Sekido, M. (2010). VLBI Data Interchange Format (VDIF). In *IVS 2010 General Meeting Proceedings*, pp. 192–196. NASA/CP-2010-215864.

Whitney, A. R., Rogers, A. E. E., Hinteregger, H. F., Knight, C. A., Levine, J. I., Lippincott, S., et al. (1976). A very-long-baseline interferometer system for geodetic applications. *Radio Science*, *11*(5), 421–432. https://doi.org/10.1029/RS011i005p00421

Xu, M. H., Heinkelmann, R., Anderson, J. M., Mora-Diaz, J., Schuh, H., & Wang, G. L. (2016). The source structure of 0642+449 detected from the CONT14 observations. *The Astronomical Journal*, *152*(5), 151.